fire

MDPI

Article

Investigation of Microstructural Evolution in Copper Short-Circuit Melt Marks After Fire Re-Exposure

Jeong-Hwan Kim [1], Daeryeong Baek [1], Chiwoo Choi [1], Kwangmuk Park [1], Jeongchay Jeon [1], Youn-Hyun Kim [2] and Dae-Dong Lee [2,*]

[1] Electrical Safety Research Institute, Korea Electrical Safety Corporation, 121 Cheomdan 2-ro, Jeongeup-si 56212, Jeonbuk-do, Republic of Korea; kjh7384@kesco.or.kr (J.-H.K.); bdr0610@kesco.or.kr (D.B.); choichyhoo34@kesco.or.kr (C.C.); km_park@kesco.or.kr (K.P.); cameleon@kesco.or.kr (J.J.)

[2] Department of Electrical Engineering, Hanbat National University, 125 Dongseo-daero, Yuseong-gu, Daejeon 34158, Republic of Korea; yhyunk@hanbat.ac.kr

* Correspondence: ldd77@hanbat.ac.kr; Tel.: +82-10-8596-2619

Abstract

Copper melt marks recovered from fire debris may record both an initial short circuit and subsequent fire heating. This study examined how flame re-exposure changes the microstructure of primary short-circuit marks using electron backscatter diffraction (EBSD). Marks were generated at 500 A on solid copper conductors (1.5 and 2.5 mm^2) from heat-resistant polyvinyl chloride-insulated building wire. Half were then exposed to a butane flame until a visually defined metal-reflow endpoint, giving a 2 × 2 design with five independent specimens per group (n = 20). Five descriptors were assessed using specimen-level summaries, 1-Wasserstein distances, permutational multivariate analysis of variance (PERMANOVA), and supporting dispersion and sensitivity analyses. Remelting shifted the area-weighted grain-diameter distribution toward coarser grains (thermal-history $R^2 = 0.464$) and increased the area-weighted aspect ratio in both conductor sizes ($\eta^2 = 0.618$). Circularity changed in opposite directions between the conductor sizes, whereas three intragranular misorientation metrics showed no supported thermal-history effect. The grain-diameter result persisted under a common post-reconstruction small-grain cutoff, whereas the ASTM grain-size contrast depended on small-grain inclusion. These findings indicate that EBSD interpretation of fire-recovered melt marks should consider subsequent remelting and conductor size rather than rely on any single descriptor as an origin-classification criterion.

Keywords: fire investigation; copper melt mark; primary short circuit; post-fire remelting; electron backscatter diffraction; grain-size distribution; grain aspect ratio; Wasserstein distance; PERMANOVA

Check for updates

Academic Editor: Hui Zhang

Received: 31 August 2026
Revised: 6 November 2026
Accepted: 10 November 2026
Published: 12 November 2026

Copyright: © 2026 by the authors. Licensee MDPI, Basel, Switzerland. This article is an open access article distributed under the terms and conditions of the Creative Commons Attribution (CC BY) license.

1. Introduction

Electrical wiring can ignite a fire and may continue to experience thermal or electrical damage as the fire develops. Consequently, a copper melt mark recovered from a fire scene may reflect both an initial electrical event and subsequent heat exposure. The review in [1] shows that the initiation and growth of wire fires are governed by the coupled effects of conductor heating, insulation pyrolysis and combustion, the energization state, and the external heat flux; arc formation was observed experimentally in energized cables under external radiant heating once the insulation had degraded [2], and full-scale flashover experiments produced circuit failures in energized cords and cables after the insulation had been damaged or consumed [3].

Melt marks and arc beads on copper conductors have long been treated as important metallic evidence in electrical fire investigations, yet a single feature rarely shows whether a mark was produced by the electrical event that caused the fire, formed during fire growth, or altered by later heating. Porosity and oxide penetration [4], the crystal structure of carbonized residues [5], depth-resolved elemental profiles obtained by secondary ion mass spectrometry [6] and a combined assessment of appearance, sectioned microstructure and surface oxidation [7] have all been proposed as indicators. Resolidified beads and globules nevertheless occur on small-diameter copper conductors that have passed through a fire irrespective of energization [8], so the presence or external shape of a rounded bead is not by itself diagnostic.

Because the microstructure of a melt mark forms by melt flow and solidification, it is sensitive to both the short-circuit conditions and the thermal boundary conditions: primary dendrite spacing, growth velocity and undercooling varied with wire diameter [9], the metallographic characteristics of cause beads changed with short-circuit current [10], and dendritic morphology depended on overcurrent conditions [11]. Electron backscatter diffraction (EBSD) has more recently been used to quantify grain morphology, crystallographic orientation and grain-boundary characteristics of copper melt marks: primary and secondary arc beads and flame-melted globules were compared in [12], the Σ3 boundary fraction and the normalized maximum grain size were added in [13], and their transferability was examined using marks from a fire reproduction experiment [14]. Machine-learning classifiers built on metallurgical morphology nevertheless failed to separate cause and victim beads from real fires reliably [15].

The thermal environment has also been addressed, but mostly for heat applied before or during the short circuit: in [13] the beads compared by EBSD were short-circuited at 25, 600 and 900 °C, so the elevated temperature preceded bead formation. Elsewhere, the metallographic structure and oxidation characteristics of cause beads changed progressively with the thermal environment, with loss of the original bead pattern at high exposure [16]; copper already affected by a short circuit changed again under additional flame [17]; quantitative metallography was applied to melt traces formed under short-circuit and fire conditions [18]; and [19] placed continued fire impingement outside its scope. The microstructure of an existing short-circuit mark can therefore be altered by subsequent fire exposure, so the final residue may not preserve a unique record of the initial electrical event.

Recent work has not closed this gap. A review of cable and wire fire characteristics restates how strongly ignition and flame spread depend on the insulation material, the cable configuration and the surrounding thermal environment [20]; melt marks recovered from the same real fire scene have been found to differ in microstructure [21]; and controlled experiments on copper-clad aluminum conductors showed that the microstructure and elemental composition of a melting mark depend on the cooling route and on subsequent heating to 450 and 650 °C as well as on the fault current [22]. Conductors pre-heated through a poor connection before the short circuit also yield significantly higher low-angle misorientation fractions than conductors short-circuited at room temperature [23], so thermal history preceding bead formation is itself recorded in the EBSD response. These contributions concern heat applied before or during mark formation, or marks of unverified provenance. For a mark of known primary origin that is subsequently remelted by fire, the combined influence of post-formation flame remelting and conductor cross-section on specimen-level EBSD descriptor distributions has not been quantified within a controlled factorial design. This defines the interpretive limits of microstructural evidence recovered after a fire rather than a stand-alone origin-classification criterion.

The present study uses a 2 × 2 factorial experiment on 1.5 and 2.5 mm^2 solid copper conductors from heat-resistant polyvinyl chloride-insulated building wire (HIV). Primary

short-circuit melt marks were compared with independently prepared primary marks subsequently remelted and resolidified by an external flame. Rather than proposing a single diagnostic threshold or a fire-origin classifier, we evaluated how the final microstructure changes with post-formation thermal history and whether the response depends on conductor cross-section.

Five descriptors were selected to characterize grain size (grain diameter and ASTM grain-size number [24]), grain shape (aspect ratio and circularity), and local crystallographic misorientation (kernel average misorientation, KAM). These specimen-level distributions were compared using the 1-Wasserstein distance, factorial permutational multivariate analysis of variance (PERMANOVA), and supporting dispersion and sensitivity analyses. Together, these analyses assess how fire re-exposure and conductor cross-section may affect the interpretation of microstructural evidence.

2. Materials and Methods

2.1. Study Concept and Experimental Design

This study evaluated how flame-induced remelting and resolidification affect the microstructure of a previously formed primary short-circuit melt mark. The final microstructure may reflect both the initial electrical event and subsequent fire heating; therefore, the experiment was designed to compare these histories under controlled conditions.

The experimental factors were conductor cross-sectional area (1.5 and 2.5 mm^2) and post-short-circuit thermal history: a melt mark produced by a primary short circuit (P) and a primary mark subsequently remelted and resolidified by an external flame (R). Five independently prepared specimens were analyzed in each condition, giving 20 in total. Ten specimens were retained as primary (P) melt marks, whereas the other ten were independently generated in separate short-circuit tests and subsequently exposed to a flame to form the remelted (R) groups. No specimen assigned to a P group was reused in an R group. The study concept and the 2 × 2 design are summarized in Table 1.

Table 1. Experimental design and specimen allocation (2 × 2 factorial).

Group	Conductor Cross-Section	Thermal History	Independent Specimens (n)
1.5-P	1.5 mm^2	Primary short-circuit only (no subsequent flame exposure)	5
1.5-R	1.5 mm^2	Primary short-circuit followed by flame remelting and resolidification	5
2.5-P	2.5 mm^2	Primary short-circuit followed by flame remelting and resolidification	5
2.5-R	2.5 mm^2	Primary mark followed by flame remelting and resolidification	5

The test material was 600 V-class HIV solid copper building wire, with nominal conductor cross-sections of 1.5 and 2.5 mm^2 corresponding to equivalent solid-wire diameters of approximately 1.38 and 1.78 mm. All specimens were prepared from commercial building wire supplied by the same manufacturer to minimize variation due to the material source.

The insulation was completely removed over the section where the short circuit and the subsequent flame exposure took place, so the tests were performed on bare conductors. This minimized the influence of insulation pyrolysis, charring and combustion products on the melting and solidification behaviour of the copper and on the EBSD results. The experiment therefore does not reproduce every thermal and chemical condition of a real fire scene but isolates how the final microstructural evidence is reconstructed when a primary melt mark is remelted by subsequent fire heat. In this experiment, the R groups consisted of pre-existing primary short-circuit melt marks subsequently exposed to external flame, without a second electrically induced short circuit; the purpose was to quantify post-formation thermal alteration of known primary marks (Section 4.5).

2.2. Primary Short-Circuit Melt-Mark Generation

Primary melt marks were generated using a 220 V, 60 Hz alternating-current (AC) supply by momentarily bringing the stripped ends of two copper wires into contact. The test circuit consisted of a distribution panel, a resistive current-limiting device, a short-circuit tester holding the two bare copper wires, a current probe and a digital oscilloscope (Figure 1). Contact was made with a remotely actuated mechanism so that the wire ends met end to end, which reduced operator-dependent variation in the instant of short-circuit initiation and in the contact condition.

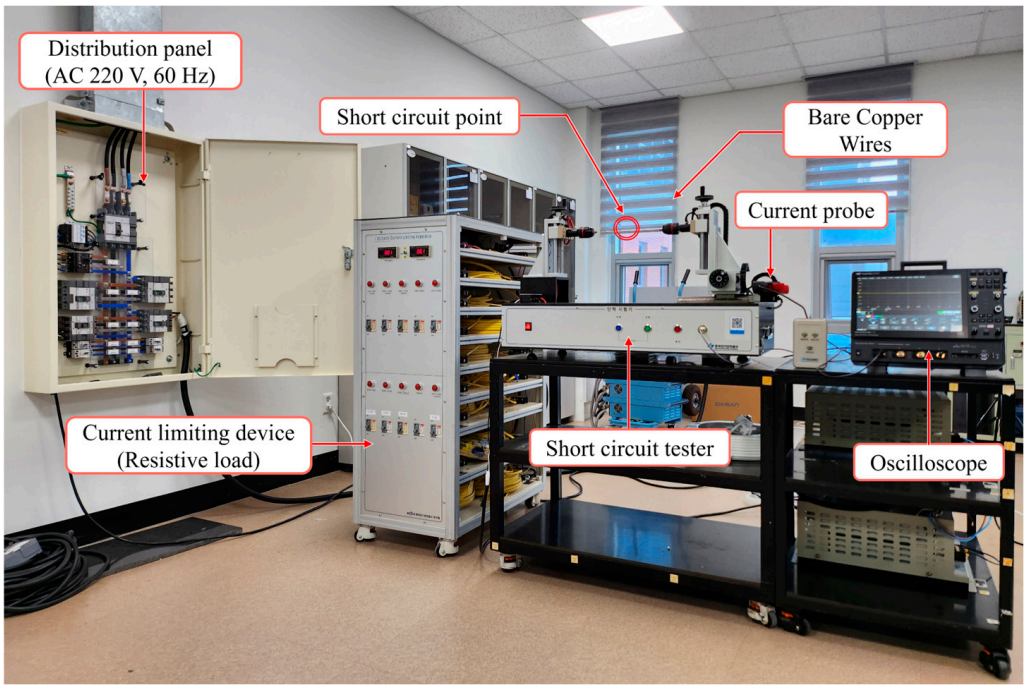

Figure 1. Short circuit test apparatus.

The short-circuit current was set to a target value of 500 A with an acceptance range of ±3%. Current was measured with a current probe (A621, Tektronix, Beaverton, OR, USA). The current was recorded using a digital oscilloscope (WaveSurfer 4024HD, Teledyne LeCroy, Chestnut Ridge, NY, USA) at a sampling rate of 50 MS/swith a record length of 10 million points per channel, corresponding to a 200 ms capture window (20 ms/div), a vertical scale of 200 A/div, and direct-current (DC) coupling. The same protective-device type, rating, and operating settings were used to interrupt the circuit in all 20 tests, so interruption conditions were nominally consistent without imposing an identical current duration; complete current waveforms (short-circuit onset to final extinction) were stored for every test, always within the 200 ms acquisition window, but duration itself was not extracted as a quantitative variable or used as a covariate in the statistical analysis. Formation of a primary melt mark was defined as the appearance of a metallic molten globule or of a clearly localized melted and resolidified region after the short circuit.

2.3. Post-Short-Circuit Flame Exposure and Remelting Criterion

Specimens of the remelted group were prepared by forming a primary melt mark as described in Section 2.2 and then applying an external flame directly to that mark, representing a melt mark exposed to an additional heat source while the fire grows or persists. A commercially available butane gas torch was used in ambient air for all specimens; its nominal maximum flame temperature of approximately 1300 °C is a burner rating and is

not treated as a measured copper temperature. The wire was held in insulated tongs, and a positioning jig was used to maintain a consistent stand-off distance and flame incidence direction between the butane torch and the melt mark throughout the flame-exposure tests (Figure 2).

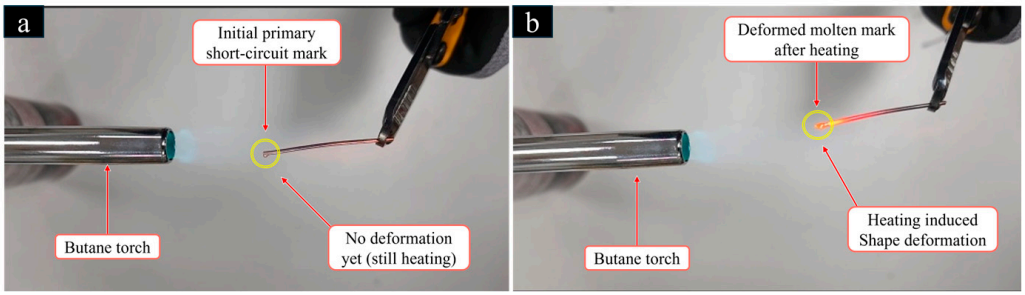

Figure 2. The operational metal-reflow endpoint: (**a**) before; (**b**) at the endpoint.

Rather than fixing a single exposure time, an operational endpoint based on the observable state of the metal was used. Surface discoloration or incandescence alone was not accepted as remelting: in Figure 2a the mark is being heated but remains faceted with its outline unchanged, so the endpoint has not been reached. The endpoint was assigned only when continuous rounding of the melt-mark surface, rearrangement of the molten region and a clear change in the original bead outline were observed together, as in Figure 2b. For all ten specimens in the remelted group, the operational metal-reflow endpoint was identified from directly observed, visible movement of metallic material and substantial deformation and collapse of the original bead contour, rather than from surface discoloration or incandescence alone; however, these observations did not quantify the molten fraction or demonstrate that the entire bead was fully liquid at the same time. Because this endpoint was visually defined rather than time-fixed, the flame-exposure duration varied between approximately 50 and 70 s (typically about 60 s). The flame was then removed, and the specimens were allowed to cool naturally in laboratory air without quenching or forced convection.

The paired macrographs of Figure 3 are shown at the same magnification with the conductor axis horizontal and the conductor to the left; the top row is 1.5 mm^2 and the bottom row 2.5 mm^2. Panels (a,d) show a primary melt mark of a groupP specimen, panels (b,e) a remelted-group specimen before flame exposure, and panels (c,f) the same specimen after the flame was removed at the endpoint. In both cross-sections the angular, faceted outline of the primary mark is replaced by a smooth, near-spherical bead with a distinct neck at the junction with the unmelted conductor, and the surface changes to a dark, thick oxide. The paired pre- and post-exposure photographs corroborate the substantial change in bead morphology, while the motion of the metal was observed directly during heating rather than recorded continuously. These photographs are therefore best interpreted as qualitative evidence, offering limited quantitative insight into the depth of melting, the liquid fraction, or the completeness of melting.The internal time–temperature history, heat flux, temperature gradient, solidification rate and melt fraction were not measured, so the nominal torch temperature is not used to infer the metal temperature. The condition is therefore described throughout as post-short-circuit remelting resolidification identified by an operational metal-reflow endpoint.

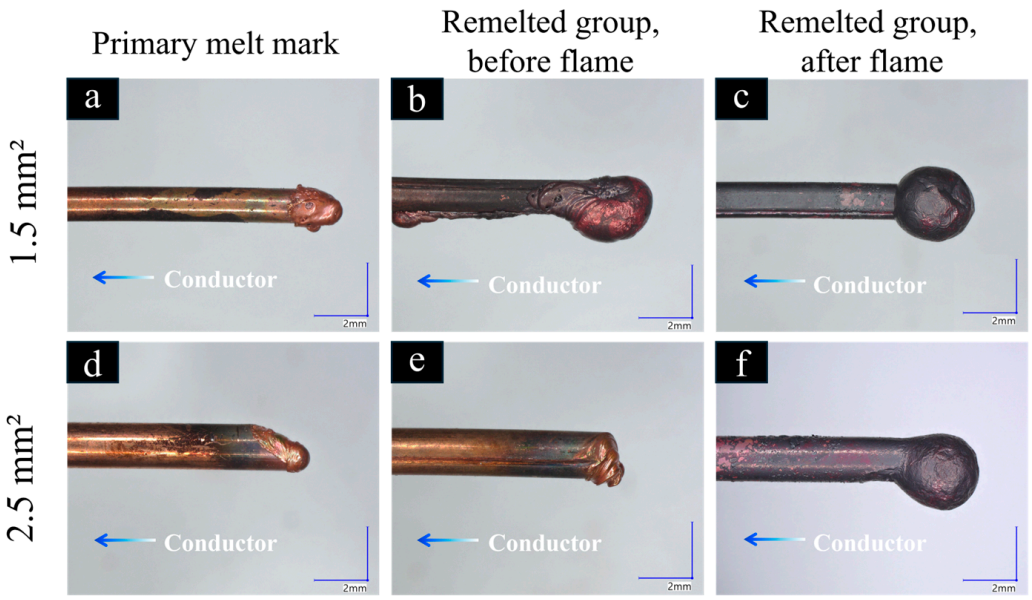

Figure 3. Melt marks before and after flame remelting: (**a**,**d**) primary mark; (**b**,**e**) remelted group before flame; (**c**,**f**) remelted group after flame.

2.4. Longitudinal Sectioning and Metallographic Preparation

Each melt mark was sectioned along a longitudinal plane parallel to the wire axis so that the melted and resolidified region and the adjacent unmelted conductor were exposed on a single analysis surface (Figure 4). On the OP-S-etched section the parent conductor, to the left in Figure 4, retains the equiaxed, twinned structure of the drawn wire and was not analyzed, whereas the melted zone to the right of the dashed fusion boundary is distinguished by its rounded contour and by entrapped gas porosity characteristic of solidification from the melt. The box indicates the type, position and approximate size of the EBSD region of interest (ROI); it is schematic and does not reproduce the exact acquisition field of any individual specimen (Section 2.5).

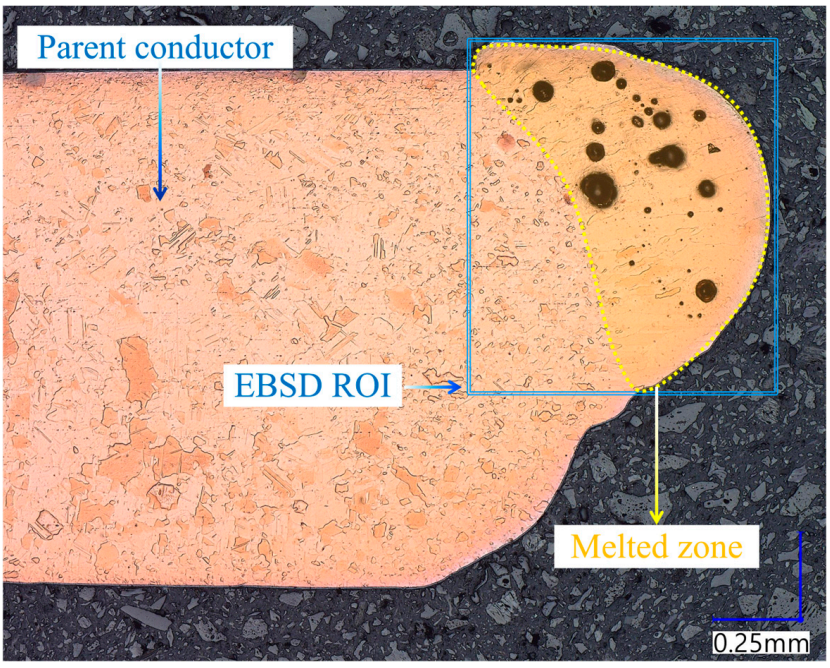

Figure 4. Longitudinal section of a copper melt mark with the EBSD region of interest.

Sectioned specimens were hot-mounted in 25 mm diameter PolyFast conductive resin using a mounting press (CitoPress-30, Struers, Ballerup, Denmark) at 180 °C and 250 bar, with 3 min heating and 2.5 min cooling. Surfaces were prepared on an automatic grinding and polishing system (Tegramin-20, Struers, Ballerup, Denmark) by grinding with 800, 1200 and 2400 grit SiC paper (Struers, Ballerup, Denmark), stepwise polishing with 6, 3 and 1 µm diamond suspensions (Struers, Ballerup, Denmark), and a final chemical-mechanical polish with OP-S colloidal silica (Struers, Ballerup, Denmark), which also served as the etchant that reveals the microstructure (no separate chemical etching was applied), with cleaning and drying after each step. Representative image-quality maps and inverse pole figure (IPF) orientation maps obtained after this sectioning and polishing procedure are shown for all four experimental groups in Figure 5.

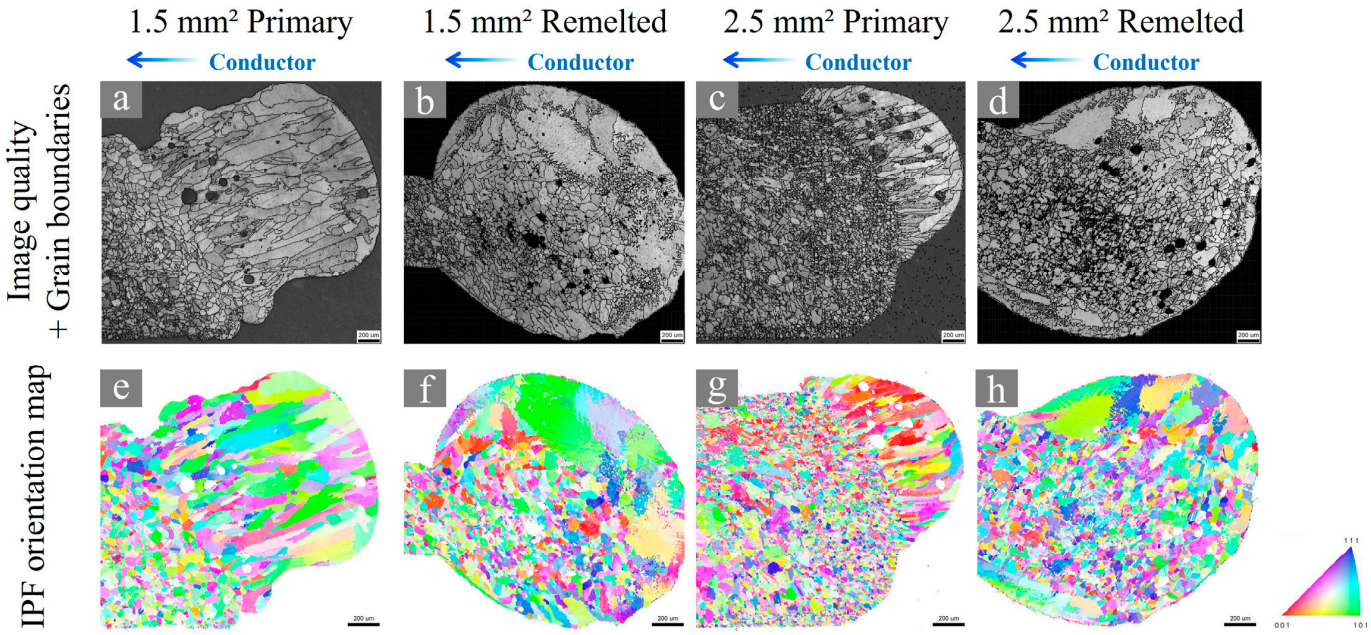

Figure 5. Representative EBSD maps of the four experimental groups: (**a**–**d**) image-quality maps with reconstructed grain boundaries and (**e**–**h**) IPF orientation maps. Scale bars: 200 µm.

2.5. EBSD Acquisition and Region-of-Interest Selection

The crystallographic microstructure was analyzed with an EBSD detector (Velocity Super, EDAX, Mahwah, NJ, USA) mounted on a field-emission scanning electron microscope (FE-SEM; GeminiSEM 460, ZEISS, Oberkochen, Germany). Data acquisition and post-processing were performed using APEX software (version 3.0, EDAX, Mahwah, NJ, USA) and orientation imaging microscopy (OIM) Analysis software (version 9.1, EDAX, Mahwah, NJ, USA). All specimens were acquired under a common EBSD protocol (15 kV accelerating voltage, 30 nA probe current, 70° tilt, 14–17 mm working-distance range, and 4 µm step size). Identical grain-reconstruction settings were used for all datasets, including a 5° grain tolerance angle, a minimum grain size of two indexed points, and no neighbour-orientation-based cleanup that would modify grain shape. Because these settings were identical for every specimen, the smallest grain that could be reconstructed was also identical for every specimen, corresponding to the circle-equivalent diameter of a two-point grain at a 4 µm step on a hexagonal grid, approximately 5.94 µm. Grain-size summaries weighted by grain number nevertheless depend on how many of the finest reconstructed grains a given microstructure contains, and a coarser microstructure contains proportionally fewer of them. Because this dependence acts in the same direction as the effect of interest, its influence was quantified rather than assumed, using a post-reconstruction sensitivity analysis in

which a single common cutoff was applied identically to the already reconstructed data of both groups (Sections 2.7 and 3.6). The absolute scan window was allowed to vary with melt-mark geometry rather than forcing the same rectangular field onto every specimen.

The ROI was placed inside the melted and resolidified region, with its inner edge at the fusion boundary—identified on the sectioned surface by the onset of the columnar solidification structure and by entrapped gas porosity—and extended toward the outer surface of the bead (Figure 4). The parent conductor and transition region were excluded, as were mounting resin, large pores, heavily oxidized areas, pull-out and regions of concentrated polishing damage. The fusion boundary provided a practical microstructural reference for distinguishing the selected resolidified region from adjacent parent-conductor material. Because melt-mark size and shape differed between specimens, an identical absolute scan area was not imposed; the same inclusion and exclusion criteria were applied to every mapped region. Accordingly, the reported distributions characterize the selected two-dimensional resolidified ROI of each specimen; they do not establish the microstructure of the entire melt-mark cross-section or its three-dimensional volume.

For orientation reliability, measurement points with a confidence index (CI) below 0.1 were excluded from the quantitative analysis. KAM was calculated for the first nearest neighbours using the same first-neighbour definition and a 5° misorientation cutoff for every dataset, so neighbour pairs misoriented by more than 5° from the central point were excluded and KAM mainly reflects local orientation heterogeneity within grains. Nevertheless, the KAM results remain subject to the spatial sampling and indexing limitations of the common EBSD protocol and are interpreted within those limitations. Figure 5 shows, for each group, the image-quality map with reconstructed grain-boundary overlays and the corresponding IPF orientation map of the same field, all rotated with the unmelted conductor toward the left.

2.6. EBSD Descriptors and Empirical Distribution Construction

Five core EBSD descriptors were selected to represent grain size, grain shape, and local orientation heterogeneity with limited redundancy. Grain diameter and the ASTM grain-size number [24] characterize grain size. Grain aspect ratio and circularity describe complementary aspects of grain shape, whereas KAM characterizes intragranular orientation variation. The five descriptors are not analyzed in the same way: grain diameter, ASTM grain size, circularity and KAM are exported as per-specimen histograms and analyzed at the distribution level (Section 2.7). Grain aspect ratio was selected on the same basis as the other four descriptors, but its exported histogram was number-weighted whereas the reported outcome was the area-weighted mean, so it was evaluated at the level of independent specimens using two-way analysis of variance (ANOVA). This difference in statistical representation explains the original separation from the four distribution-level Wasserstein/PERMANOVA analyses, but it does not, by itself, justify excluding the related hypothesis from multiple-testing considerations. A conservative multiplicity sensitivity calculation is therefore specified in Section 2.7. Two further misorientation metrics exported by the same software, grain average misorientation (GAM) and local orientation spread (LOS), were retained as specimen-level checks on KAM, and the maximum reconstructed grain diameter was retained because it is related to, but not identical with, the normalized maximum grain size proposed as a discriminant parameter in [13], which is defined as the area of the largest grain divided by the total area of the molten mark.

The histogram of each independent specimen was constructed from 50 common bin centres and the corresponding number or area fractions. The empirical distribution of descriptor k for specimen i was expressed as

$$P_{ik}(x) = \sum_{b=1}^{50} w_{ikb}\delta(x - x_{kb}) \quad (1)$$

where x_{kb} is the *b-th* bin centre of descriptor k, w_{ikb} is the relative fraction in that bin and δ is the Dirac delta. To remove the small rounding errors introduced during spreadsheet export, each specimen distribution was renormalized before analysis as

$$\tilde{W}_{ikb} = \frac{w_{ikb}}{\sum_{b=1}^{50} w_{ikb}} \quad (2)$$

so that the weights of every specimen sum to unity. The independent experimental unit was defined as one independently prepared copper wire specimen and not as an individual grain or EBSD pixel. The number of independent samples per group is therefore n = 5 and the total is N = 20. Grain- and pixel-level observations were used only to estimate the empirical microstructural distribution of each specimen and were not treated as additional independent replicates.

2.7. Distribution-Level Statistical Analysis

Specimen-level means and medians were first tabulated for each descriptor to describe the basic trends of the four groups. To quantify shifts of the complete EBSD distribution that a single summary value cannot express, the 1-Wasserstein distance (W_1) was then used; this is the transport-based two-sample statistic whose relationships to the classical distribution-free tests are set out in [25]. For the cumulative distribution functions and of two specimens, was calculated as

$$W_1(P_i, P_j) = \int |F_i(x) - F_j(x)|dx \quad (3)$$

All pairwise W_1 values among the 20 independent specimens were computed for each descriptor to build a 20 × 20 distance matrix. Because W_1 retains the original unit and scale of the descriptor, raw distance values were not compared between descriptors as effect sizes.

The balanced 2 × 2 factorial design included five independently prepared specimens per experimental group (N = 20). No a priori power analysis, simulation-based sample-size calculation, or prespecified minimum detectable effect was used to determine this sample size. Consequently, sample-size adequacy for detecting thermal-history or interaction effects was not established before the experiments, and the statistical findings are interpreted as exploratory observations under the conditions investigated.

To separate the effects of conductor cross-section and post-short-circuit thermal history, the following 2 × 2 factorial PERMANOVA [26] model was applied to each Wasserstein distance matrix:

$$D_k \sim T + C + T \times C \quad (4)$$

where D_k is the specimen-level Wasserstein distance matrix of descriptor k, T is thermal history (primary versus remelted), C is conductor cross-sectional area (1.5 versus 2.5 mm^2) and T × C is their interaction. Pseudo-F, a permutation-based p value and the explained variance R^2 were obtained for each term, with 9999 permutations of the 20 independent specimen labels.

To assess whether differences in group dispersion could influence the PERMANOVA findings, we performed PERMDISP [27]. For each distance matrix, dispersion was estimated from the distances of specimens to their group centroids in principal-coordinate space. A PERMANOVA result can reflect differences in group locations, group dispersions,

or both; therefore, the two analyses were interpreted together. Benjamini–Hochberg false discovery rate (BH-FDR) correction [28] was applied to the tests of the four distribution-level descriptors. The specimen-level area-weighted aspect-ratio ANOVA was originally reported outside that family. To assess the sensitivity of its thermal-history result to a broader multiplicity definition, a conservative Bonferroni calculation was additionally applied to the reported nominal p value using 15 factorial tests (five principal EBSD descriptors × three terms: thermal history, conductor cross-section, and their interaction). The approximate adjusted value was calculated as $\min(15 \times p, 1)$. This calculation uses the rounded reported p value and does not represent a recalculated combined BH-FDR q value or adjustment across all ancillary analyses. With 9999 permutations, the smallest attainable permutation p value is 1×10^{-4}, and the balanced 5/5/5/5 design admits $20!/(5!)^4$ distinct label assignments. These values describe p-value resolution and the size of the permutation space, not statistical power.

To show where within the distribution the changes occurred, quantile differences between the remelted and primary conditions were computed over the 10th–90th percentile range as

$$\Delta Q(p) = Q^{R}(p) - Q^{P}(p) \quad (5)$$

A positive ΔQ indicates that the corresponding quantile increased after remelting and a negative value that it decreased. The uncertainty of each shift was expressed as a 95% confidence interval from 10,000 specimen-level non-parametric bootstrap resamples. These intervals visualize position-dependent change and were not used as hypothesis tests replacing the factorial PERMANOVA.

As a descriptive indicator of the thermal-history effect relative to specimen-to-specimen variation, a separation ratio was calculated for each cross-section and descriptor as the mean W_1 between primary and remelted specimens divided by the pooled mean pairwise W_1 within the two conditions. A ratio above one means that the mean distance between different thermal histories exceeds that between specimens sharing the same history. It is a descriptive contrast measure, not a classification accuracy or a diagnostic threshold.

A leave-one-specimen-out (LOSO) sensitivity analysis checked whether any single specimen dominated the results. Each of the 20 specimens was removed in turn and the Wasserstein matrix and factorial PERMANOVA were recomputed, giving the range of R^2 for each term and confirming that the direction of the effects was retained. LOSO evaluated the sensitivity of effect-size estimates to the omission of an individual specimen, whereas the 10,000 specimen-level bootstrap resamples characterized uncertainty in quantile shifts. Neither procedure created additional independent observations.

To test sensitivity to the inclusion of small grains, a common post-reconstruction grain-diameter cutoff of 7.425 µm was applied identically to both groups. This value is 1.25 times the smallest grain diameter that the common acquisition and reconstruction protocol can resolve (Section 2.5) and was chosen as a conservative threshold spanning the diameter range over which the two groups differ most in small-grain number density. For the ASTM grain-size distributions, grains below the cutoff were excluded, the retained distributions were renormalized, and specimen summaries and factorial PERMANOVA were recomputed. For the area-weighted grain-diameter analysis, the entire lowest diameter histogram bin was conservatively excluded before reanalysis. Neither procedure involved repeating EBSD indexing or grain reconstruction; the latter was a bin-based sensitivity check rather than an exact grain-by-grain 7.425 µm exclusion. Sums of squares were partitioned sequentially, which is exact for the balanced full dataset and was retained in the LOSO analysis so that the reported ranges remain comparable with the full-sample values.

2.8. Quality Control and Reproducibility

Specimens were included only when they met the pre-defined electrical, remelting, metallographic and EBSD quality criteria stated in Sections 2.2–2.5, and descriptor selection, binning, normalization, distance calculation and the permutation procedure were identical for all 20 specimens. Experimental consistency was further supported by separate short-circuit preparation of each specimen, identical remote-contact and protective-device settings, and, for the R groups, the same torch-positioning jig and operational metal-reflow endpoint. These procedural controls did not ensure identical internal thermal histories. As in Section 2.7, PERMANOVA R^2 values—rather than raw Wasserstein distances—were used for comparing effect sizes between descriptors.

3. Results

EBSD microstructural changes associated with conductor cross-section and post-short-circuit flame remelting were compared across 20 independent specimens (n = 5 per group). Sections 3.1–3.5 present these results in turn, and Section 3.6 reports a sensitivity analysis for the grain-size findings.

3.1. Representative Observations and Group-Level Differences After Remelting

Representative observations are consistent with the group assignments used in the quantitative analysis: the paired macrographs show substantial contour rearrangement and oxide development after flame exposure (Figure 3), the sectioned mark shows a resolidified region clearly distinguishable from the parent conductor (Figure 4), and the image-quality and IPF maps show pronounced spatial heterogeneity in all four groups, with a band of fine, near-equiaxed grains on the conductor side and coarser, elongated grains extending toward the interior and outer surface of the bead (Figure 5). These images are illustrative and were not counted as additional replicates.

Figure 6 and Table 2 summarize the EBSD descriptors at the specimen level. Mean grain diameter increased from 88.42 ± 22.07 to 105.18 ± 24.70 μm (+19.0%) at 1.5 mm^2. At 2.5 mm^2, it increased from 51.35 ± 11.44 to 123.82 ± 13.83 μm (+141.1%). The maximum reconstructed grain diameter increased by 20.2% and 189.8% at 1.5 and 2.5 mm^2, respectively. Within the two tested conductor sizes, the larger relative grain-diameter change at 2.5 mm^2 reflects a stronger response to the remelting protocol. However, because the primary-group mean diameters differed before flame re-exposure (88.42 μm at 1.5 mm^2 versus 51.35 μm at 2.5 mm^2), the percentage contrast alone does not isolate a specific geometric or solidification mechanism, nor does it establish how the response would scale to other conductor sizes. The two shape descriptors behaved differently: the area-weighted aspect ratio increased in both cross-sections, by 23.4% at 1.5 mm^2 and 21.7% at 2.5 mm^2, whereas circularity increased by 12.5% at 1.5 mm^2 but decreased by 23.5% at 2.5 mm^2, reversing direction with cross-section (examined in Section 3.5). KAM changed by +3.4% and −12.5%, with more overlap between individual specimen values than for any grain-size descriptor. The ASTM grain-size number decreased in both cross-sections, by 6.8% and 13.4%, respectively; however, this number-weighted contrast proved sensitive to the exclusion of the smallest reconstructed grains and should be interpreted together with the post-reconstruction analysis in Section 3.6. Table 2 values are specimen-level means reported by the OIM software; the distribution-level values quoted in Section 3.6 are recomputed from the 50-bin histograms and differ by less than 0.02 ASTM units. Formal inference is given in Sections 3.4 and 3.5.

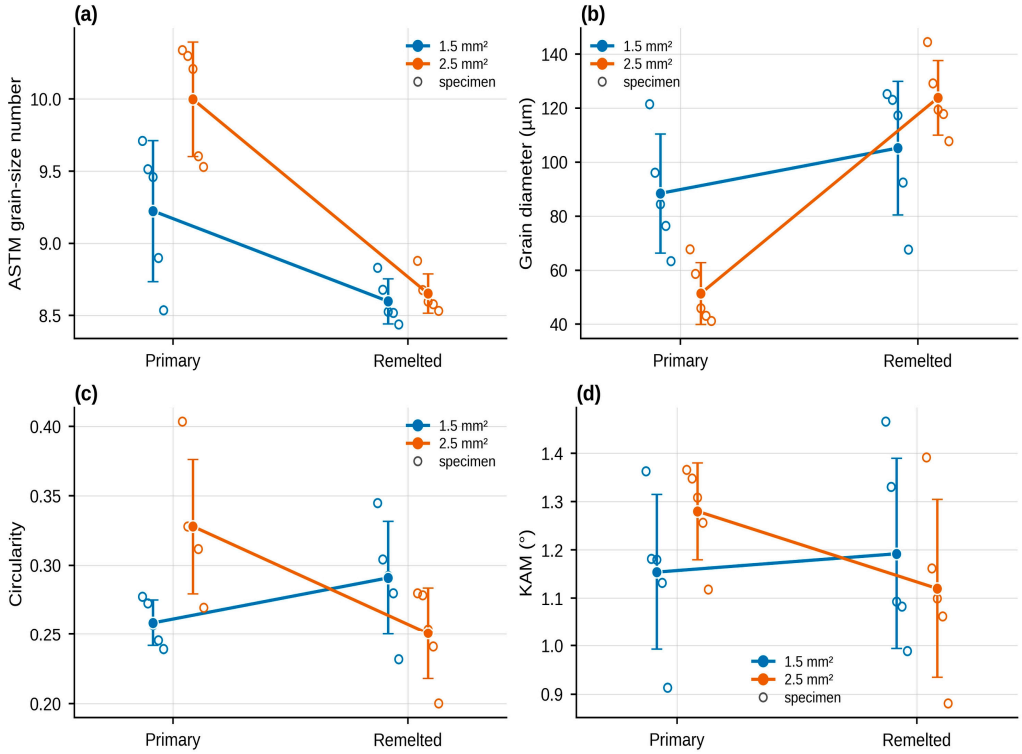

Figure 6. Specimen-level EBSD descriptors: (**a**) ASTM grain-size number, (**b**) grain diameter, (**c**) circularity, and (**d**) kernel average misorientation (KAM).

Table 2. Specimen-level summary statistics and relative changes after flame remelting.

Descriptor	1.5-P	1.5-R	Δ 1.5 (%)	2.5-P	2.5-R	Δ 2.5 (%)
ASTM grain size	9.224 ± 0.488	8.599 ± 0.157	−6.8	9.997 ± 0.396	8.653 ± 0.137	−13.4
Grain diameter (µm)	88.42 ± 22.07	105.18 ± 24.70	+19.0	51.35 ± 11.44	123.82 ± 13.83	+141.1
Circularity	0.2585 ± 0.0167	0.2909 ± 0.0408	+12.5	0.3280 ± 0.0484	0.2508 ± 0.032	−23.5
KAM (°)	1.154 ± 0.161	1.192 ± 0.198	+3.4	1.280 ± 0.100	1.120 ± 0.185	−12.5
Aspect ratio (area-weighted)	0.493 ± 0.073	0.608 ± 0.024	+23.4	0.524 ± 0.053	0.638 ± 0.018	+21.7
Maximum grain diameter (µm)	253 ± 86	304 ± 60	+20.2	142 ± 35	412 ± 58	+189.8

3.2. Distribution-Level Redistribution After Remelting

Group means can hide changes in distribution shape, so the complete per-specimen distributions were examined next. Figure 7 shows the group-level empirical distributions as the mean of the five specimens of each group, with shaded bands indicating ±1 standard deviation and dashed and solid curves for the primary and remelted conditions. Grain diameter shifted toward larger values in both cross-sections; at 2.5 mm^2 the pronounced fine-grain peak of the primary condition largely disappeared, and the area was redistributed toward coarser grains with a markedly expanded right tail. Circularity shifted higher at 1.5 mm^2 and lower at 2.5 mm^2, whereas the KAM distributions of the four groups overlapped substantially. Differences near the fine-grain end of the ASTM distributions were examined by applying a common post-reconstruction diameter cutoff in Section 3.6.

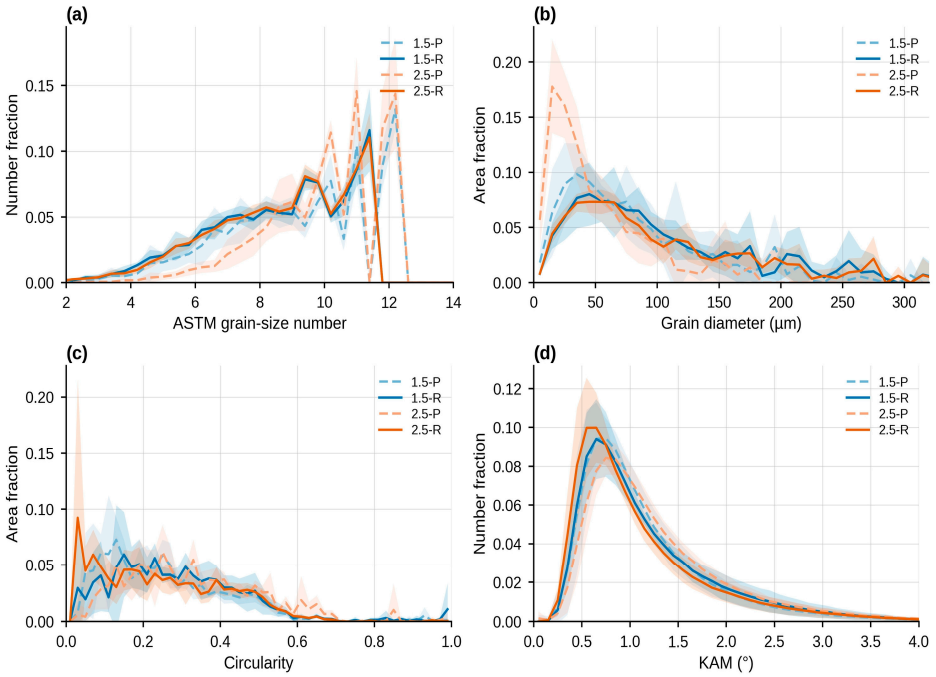

Figure 7. Group-level empirical distributions: (**a**) ASTM grain-size number; (**b**) grain diameter; (**c**) circularity; (**d**) KAM.

To locate the remelting effect within the distributions, remelted–primary differences were calculated at the 10th–90th quantiles with specimen-level bootstrap 95% confidence intervals (10,000 resamples; Figure 8). The ASTM change was negative at every quantile in both cross-sections, and grain diameter was positive throughout, rising at 2.5 mm^2 to about +160 μm at the 90th percentile. Circularity remained positive at 1.5 mm^2 and negative at 2.5 mm^2, while KAM showed smaller changes with intervals including zero over most of the range.

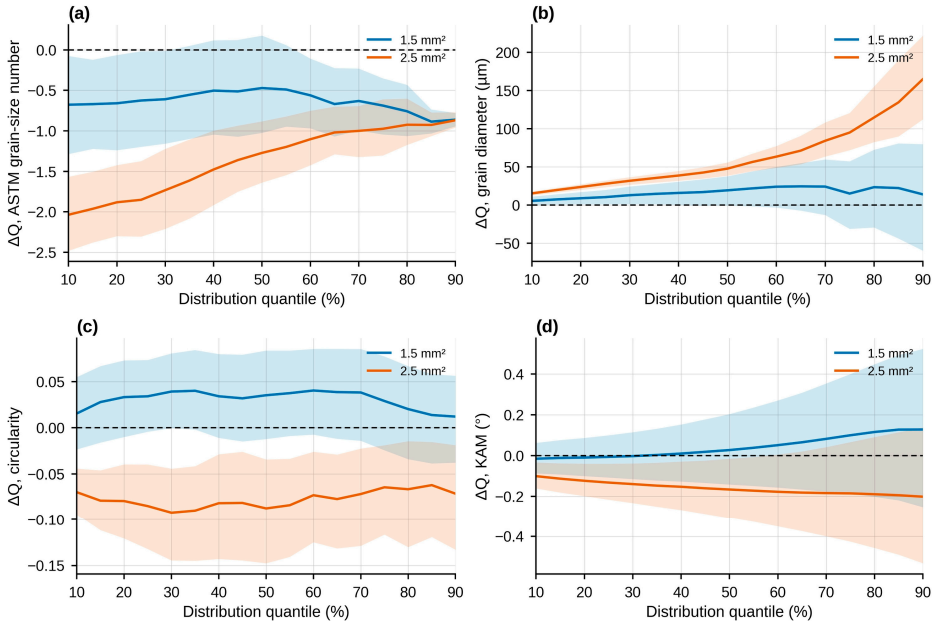

Figure 8. Quantile shift ΔQ between the remelted and primary conditions: (**a**) ASTM grain-size number; (**b**) grain diameter; (**c**) circularity; (**d**) KAM.

3.3. Thermal-History Contrast Relative to Specimen Variability

To assess whether the observed differences exceed the variability between specimens of the same condition, the mean primary–remelted Wasserstein distance was compared with the mean pairwise distance within the same thermal history (Figure 9). For grain diameter, the separation ratio was 1.01 at 1.5 mm^2 but 3.84 at 2.5 mm^2; the corresponding values were 1.70 and 4.00 for ASTM grain size, 1.07 and 1.54 for circularity, and 0.89 and 1.22 for KAM. The extent to which a change exceeded within-condition variability therefore varied considerably across descriptors and conductor cross-sections. This is a relative contrast, not a diagnostic threshold.

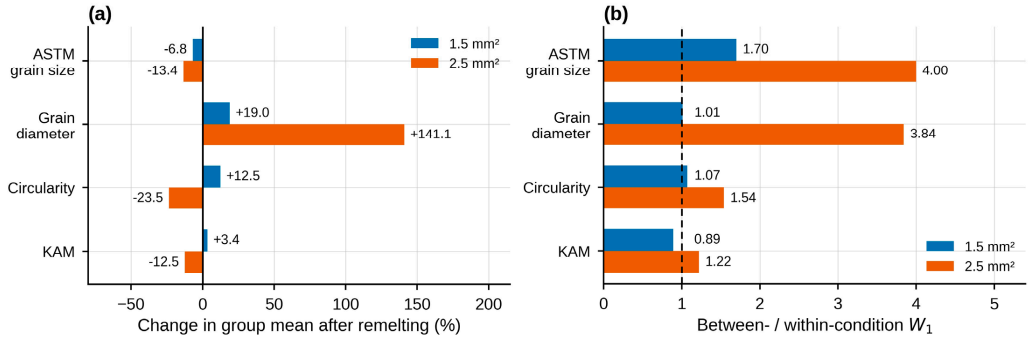

Figure 9. Remelting contrast of the EBSD descriptors: (**a**) relative change in group means; (**b**) between- to within-condition W_1 ratio.

3.4. Thermal-History, Conductor-Size, and Interaction Effects

The factorial PERMANOVA results are given in Table 3 and Figure 10. Grain diameter showed a large thermal-history effect ($R^2 = 0.464$, BH-FDR-adjusted $q = 0.0006$) together with an interaction ($R^2 = 0.192$, $q = 0.0132$). For circularity, the interaction exceeded either main effect ($R^2 = 0.305$, $q = 0.0132$), and for KAM no term survived BH-FDR correction. The ASTM grain-size number showed the nominally largest thermal-history effect ($R^2 = 0.600$, $q = 0.0004$), reassessed in Section 3.6. Its interaction term was also supported after correction ($R^2 = 0.077$, $q = 0.0395$). Although the original ASTM grain-size terms were statistically supported, their sensitivity to the inclusion of smaller reconstructed grains (Section 3.6), together with the ASTM PERMDISP result, limits their interpretation as stand-alone evidence of microstructural coarsening. The PERMDISP test detected significant dispersion heterogeneity among the four groups for the number-weighted ASTM grain-size distribution ($p = 0.0357$), but not for area-weighted grain diameter ($p = 0.2502$), circularity ($p = 0.4667$), or KAM ($p = 0.6103$). Because the factorial PERMANOVA terms may be influenced by both group-centroid configuration and differences in within-group dispersion, the significant ASTM thermal-history and interaction terms cannot be attributed solely to centroid separation. The present results do not quantify the relative contributions of group location and dispersion. The circularity interaction reflects opposite response directions in the two conductor sizes rather than a common shift in grain shape. Under LOSO, the thermal-history R^2 stayed within 0.433–0.589 for grain diameter and 0.580–0.733 for ASTM grain size, the interaction R^2 within 0.129–0.233 for grain diameter and 0.250–0.397 for circularity, and the thermal-history R^2 for KAM remained low at 0.017–0.103; the ranking and direction of the principal effects were retained when any single specimen was excluded.

Table 3. Factorial PERMANOVA and PERMDISP results based on specimen-level Wasserstein distances.

Descriptor	Thermal History R^2 (q)	Cross-Section R^2 (q)	Interaction R^2 (q)	PERMDISP *p*
ASTM	0.600 (0.0004)	0.103 (0.0596)	0.077 (0.0395)	0.0357
Diameter	0.464 (0.0006)	0.024 (0.3840)	0.192 (0.0132)	0.2502
Circularity	0.055 (0.3024)	0.045 (0.3840)	0.305 (0.0132)	0.4667
KAM	0.040 (0.3958)	0.008 (0.7221)	0.096 (0.1925)	0.6103

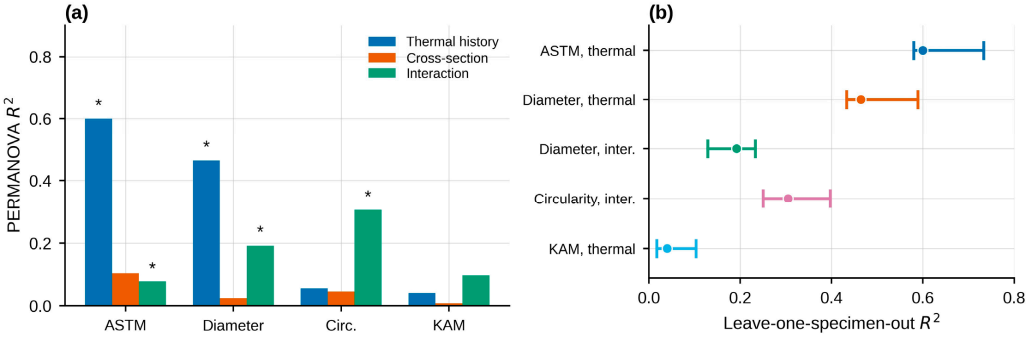

Figure 10. Factorial effects and specimen sensitivity: (**a**) PERMANOVA R^2; (**b**) leave-one-specimen-out ranges. Asterisks (*) indicate statistically significant effects based on PERMANOVA ($p < 0.05$).

These LOSO ranges describe within-dataset sensitivity to omitting one specimen. They are not confidence intervals for the factorial effects and do not demonstrate that every effect remained statistically significant under each omission or that the sample size provided adequate power. In particular, the reported interaction effects require independent replication.

3.5. Grain Morphology and the Intragranular Misorientation Family

Circularity and grain aspect ratio describe different aspects of grain shape, and Section 3.1 showed that they behaved differently. The area-weighted aspect ratio rose from 0.493 ± 0.073 to 0.608 ± 0.024 at 1.5 mm^2 and from 0.524 ± 0.053 to 0.638 ± 0.018 at 2.5 mm^2 (Figure 11a); a two-way analysis of variance showed a thermal-history effect of $\eta^2 = 0.618$ ($p = 0.0001$) with no supported interaction ($p = 0.97$), so it responded consistently in both conductors, unlike circularity, and its between-specimen standard deviation fell to about one-third of the primary value. Under the conservative 15-test Bonferroni sensitivity calculation specified in Section 2.7, applying this nominal $p = 0.0001$ gives an approximate adjusted value of 0.0015, which remains below 0.05. Because the original *p* value was rounded, this adjusted value is approximate and is not a newly calculated BH-FDR q value. No comparable thermal-history effect was supported for the number-weighted mean ($\eta^2 = 0.037$, $p = 0.34$) or the number-weighted distribution ($R^2 = 0.043$, $p = 0.30$). Thus, the morphological response is specific to the area-weighted statistic and does not demonstrate a population-wide shift among individual grains. As with the other descriptors, this observation pertains to the selected longitudinal regions examined in this study, rather than the complete three-dimensional melt-mark volume. In contrast, circularity responded in opposite directions in the two conductor sizes, as shown by the specimen-level group summaries (Table 2 and Figure 6), the empirical distributions (Figure 7), and the 10th–90th percentile shift profiles (Figure 8). These results provide complementary descriptions of the same 20 independent specimens rather than independent experimental validation of the underlying mechanism. The nonparallel behaviour of the two shape descriptors is geometrically plausible: aspect ratio primarily reflects elongation, whereas circularity is additionally sensitive to the compactness and perimeter complexity of a grain boundary.

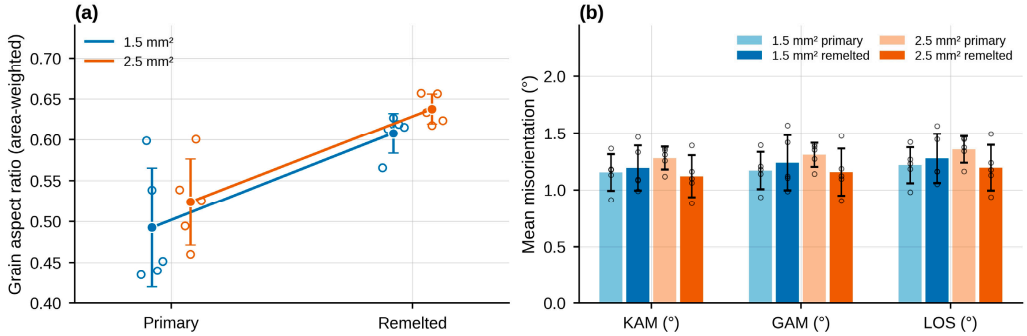

Figure 11. Grain aspect ratio and intragranular misorientation: (**a**) area-weighted grain aspect ratio; (**b**) KAM, GAM and LOS.

The absence of a KAM response was checked against two further misorientation metrics. Neither grain average misorientation nor local orientation spread showed a supported thermal-history effect (specimen-level ANOVA $p = 0.62$ and $p = 0.53$, compared with $p = 0.42$ for KAM), and the four group means of all three lay between 1.12° and 1.36° with overlapping specimen-level scatter (Figure 11b), so the null result does not depend on the KAM kernel. The correlated disorientation-angle fraction in the 55–63° window, which contains the Σ3 coincidence-site-lattice twin relationship [13], likewise showed no effect (group means 0.21–0.28, $\eta^2 = 0.030$, $p = 0.49$); this window is a proxy for, not a full analysis of, the Σ3 boundary population [29].

3.6. Post-Reconstruction Sensitivity to a Common Grain-Diameter Cutoff

Grain-size summaries may depend on the inclusion of the finest reconstructed grains, whose number density differs most between a fine and a coarse microstructure. We therefore assessed the stability of the grain-size findings by post-filtering the already reconstructed datasets, using a single conservative cutoff of 7.425 µm applied identically to both groups. As stated in Section 2.5, this cutoff is 1.25 times the smallest reconstructable grain diameter under the common protocol; it is an analytical choice rather than a measured property of either group, and no dataset was re-indexed or re-reconstructed. The cutoff was applied to the ASTM grain-size data, while the entire lowest diameter histogram bin was conservatively excluded for the area-weighted diameter analysis (Figure 12).

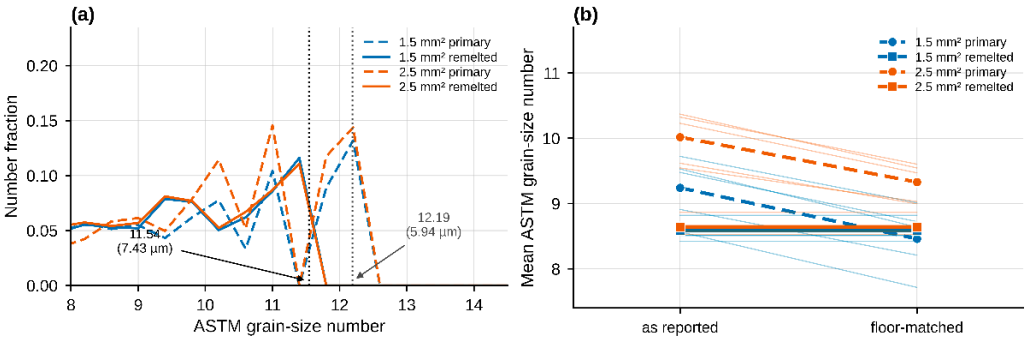

Figure 12. Post-reconstruction sensitivity to a common grain-diameter cutoff. (**a**) Mean ASTM grain-size distributions; (**b**) specimen means before and after exclusion of smaller grains.

For the ASTM grain-size number, excluding grains below 7.425 µm shifted the primary-group means by −0.78 and −0.69 units for 1.5 and 2.5 mm^2, respectively, corresponding to 125% and 51% of the original primary-to-remelted differences. After filtering, the 1.5 mm^2 contrast reversed sign to +0.155 and the 2.5 mm^2 contrast decreased in magnitude to −0.654; the thermal-history R^2 declined from 0.600 to 0.212 ($p = 0.006$). The $p = 0.006$ value is

the nominal, unadjusted result of this post-reconstruction small-grain inclusion sensitivity analysis, not a BH-FDR-adjusted q value. PERMDISP was not repeated for the filtered ASTM distributions, and therefore this sensitivity analysis does not establish dispersion homogeneity or independently verify a centroid-specific effect. In the conservative lowest-bin exclusion for area-weighted grain diameter, group means changed by less than 3%, the thermal-history R^2 changed from 0.464 to 0.453, and the interaction R^2 remained 0.192. These results support the relative robustness of the area-weighted grain-diameter finding and show that the number-weighted ASTM estimate is sensitive to the inclusion of small reconstructed grains. This behaviour reflects the dependence of number-weighted grain-size measures on the small-grain fraction, which differs between a fine and a coarse microstructure even under a common acquisition and reconstruction protocol.

4. Discussion

4.1. Principal Findings

Flame re-exposure altered some, but not all, EBSD descriptors of pre-existing primary short-circuit melt marks. The clearest changes involved area-weighted grain size and grain shape. The area-weighted grain diameter shifted toward coarser values in both conductors ($R^2 = 0.464$) with a strong interaction with cross-section ($R^2 = 0.192$), and the area-weighted grain aspect ratio rose consistently and became far more uniform between specimens ($\eta^2 = 0.618$). Grain outline compactness responded only through an interaction with conductor cross-section ($R^2 = 0.305$ for circularity, larger than either main effect), and three complementary intragranular misorientation metrics showed no factorial effect that survived correction. Although the number-weighted ASTM grain-size distribution showed a relatively large thermal-history effect in the original PERMANOVA, its interpretation is constrained by significant dispersion heterogeneity (PERMDISP $p = 0.0357$) and by sensitivity to the inclusion of the finest reconstructed grains. Accordingly, the ASTM result is treated as a descriptive observation and an example of analysis sensitivity, not as stand-alone evidence of remelting-induced grain coarsening. Previous work has compared arc-related melt marks formed under different electrical and thermal conditions [4–15] and examined thermal alteration, including exposure after initial short-circuit damage [16–18]. By comparing independently prepared primary short-circuit melt marks with groups produced using an additional flame-remelting step, the present factorial design evaluates how the final EBSD distributions depend on post-formation thermal history and conductor cross-section. This contribution concerns the stability and interpretation of microstructural evidence and does not establish a validated method for determining fire origin or event chronology.

4.2. Grain Size and Morphology After Remelting

The increase in area-weighted grain diameter was observed in both conductor sizes and was only minimally altered by the conservative lowest-bin exclusion. The quantile-shift analysis shows that this change is not confined to the mean. At 2.5 mm^2 the primary-to-remelted difference widened toward the upper quantiles and the maximum reconstructed grain diameter almost tripled, so remelting acted less as a simple translation of the distribution than as a selective expansion of the coarse-grain population. By contrast, the number-weighted ASTM grain-size result changed materially when the finest reconstructed grains were excluded. This indicates greater dependence of the ASTM summary on the small-grain fraction, without establishing that the groups were reconstructed using different settings. Where two descriptors of the same physical quantity disagree in this way, the area-weighted one is the safer basis for interpretation.

The difference between cross-sections was pronounced: the mean grain-diameter increase was 19.0% at 1.5 mm^2 but 141.1% at 2.5 mm^2, with Wasserstein separation ratios

of 1.01 and 3.84. Part of this contrast reflects the different starting points of the two primary groups, whose mean diameters were 88.42 and 51.35 µm, while the remelted groups were closer together, at 105.18 and 123.82 µm. Wire diameter is systematically related to undercooling, dendrite growth velocity and primary dendrite spacing in arc beads [9], heat extraction and thermal gradient affect the grain morphology of molten marks [12], and casting dimension affects the solid–liquid interface and final grain morphology in copper [30]. Conductor heat capacity, surface-to-volume ratio and heat-extraction path are therefore plausible contributors, but the local temperature gradient, cooling rate and melt-pool geometry were not measured here.

The two shape descriptors separated cleanly. Circularity, which reflects perimeter complexity and areal compactness rather than a simple axis ratio, increased after remelting at 1.5 mm^2 but decreased at 2.5 mm^2, and its interaction term was the largest single effect in the factorial analysis, with the quantile-shift profiles pointing in opposite directions over most of the distribution. Grain aspect ratio, which reflects elongation, increased by a similar amount in both conductors with no supported interaction and with a threefold contraction of its between-specimen scatter. Whether a shape descriptor responds in a consistent direction therefore depends on which aspect of shape it measures. A plausible explanation for the opposing circularity responses is that the two conductor cross-sections differed in their starting grain populations and in effective heat-transfer conditions during flame remelting and resolidification. Differences in thermal mass, surface-to-volume ratio, heat-extraction paths, and local melt-pool geometry may alter grain-growth competition and the complexity of reconstructed grain boundaries. This differing magnitude of grain-diameter increase (Table 2) is consistent with different magnitudes of microstructural response, but this co-occurrence does not demonstrate that coarsening caused the circularity decrease at 2.5 mm^2. The representative image-quality and inverse pole figure maps (Figure 5) illustrate microstructural heterogeneity but do not establish a specific heat-flow pattern or a cross-section-specific increase in boundary roughness. Because temperature gradients, cooling rates, solidification-front velocities, melt-pool geometries, and quantitative grain-boundary perimeter complexity were not measured, this interpretation remains a mechanistic hypothesis rather than a demonstrated causal relationship; no specific thermal-gradient-to-growth-rate (G/R) condition or columnar-to-equiaxed transition is inferred.

4.3. Intragranular Misorientation After Remelting

Unlike the area-weighted grain-size and morphology descriptors, the intragranular misorientation metrics did not respond to remelting history: the KAM mean increased slightly at 1.5 mm^2 and decreased at 2.5 mm^2, no factorial term was supported after BH-FDR correction, the separation ratio at 1.5 mm^2 was 0.89, and GAM and LOS showed the same null result. This is physically understandable, since both groups ultimately contain copper that solidified from the melt: the dislocation arrangement and orientation gradient of the previous solid structure are unlikely to survive remelting, while new gradients develop in the newly solidified grains through thermal contraction, local constraint and solidification defects. The final KAM therefore reflects lattice curvature formed after the last solidification event rather than a count of melting events. Local misorientation metrics also depend on step size and calculation kernel [31], so these absolute values should not be transferred as thresholds to other instruments, and no dislocation mechanism is inferred without transmission electron microscopy (TEM) or geometrically necessary dislocation (GND) tensor analysis.

4.4. Implications for Fire Investigation

Melt marks on conductors are important indicators of an electrical anomaly and of fire chronology, but the wire itself may be exposed to continued radiant heat, convective heat and direct flame during the fire [1–3], and a single metallurgical feature is repeatedly reported to be insufficient for determining cause [4–8,15]. The R specimens were produced by flame re-exposure and resolidification of primary short-circuit melt marks, without a second electrically induced short circuit. As secondary arc beads and other defined fire-heating histories were not included as comparator groups, the grain-size and grain-shape differences do not establish the unique origin or event sequence of an unknown fire-scene melt mark. Similar final EBSD microstructures may be compatible with multiple electrical and thermal histories; the present comparisons cannot determine the specificity of any descriptor for distinguishing those histories. Nevertheless, the changes in grain-diameter distribution and grain morphology indicate that post-formation thermal exposure may contribute substantially to the microstructure of a melt mark recovered from a real fire, so interpretation should consider possible remelting and resolidification together with the conductor specification and the thermal history of the scene.

These findings suggest that grain-shape descriptors should be interpreted together with conductor size and evidence of subsequent heating. Circularity changed in opposite directions for the two tested conductor sizes, whereas area-weighted aspect ratio changed in the same direction. This consistency makes the area-weighted aspect ratio a candidate for further study, not a validated forensic classifier. Because secondary arc beads and alternative fire-heating histories were not examined, the results do not establish thresholds for distinguishing melt-mark origins. In actual fire-scene examinations, EBSD observations should be evaluated together with independent evidence of circuit energization and protection-device operation, the estimated fire origin and spread sequence, possible subsequent heating of the conductor, macroscopic melt-mark morphology, oxide observations, and other scene findings. These types of evidence offer complementary context rather than an individually unique causal signature. Accordingly, the reported descriptors are best treated as supporting metallurgical observations, not as stand-alone indicators of melt-mark origin or of the order of electrical and thermal events. EBSD acquisition and reconstruction parameters, together with any post-reconstruction grain-inclusion thresholds, should be documented alongside the descriptors, because the inclusion of fine grains can influence number-weighted grain-size estimates (Section 3.6).

4.5. Limitations and Future Work

Several limitations apply. First, a common EBSD protocol and identical grain-reconstruction settings were applied to all 20 specimens, but the 4 μm step size sets the smallest reconstructable grain diameter at approximately 5.94 μm and therefore limits characterization of the finest grains; finer-step measurements would be needed to resolve them.

Second, only five independent specimens were analyzed per group and no a priori power analysis was performed, so the power to detect modest thermal-history effects, and particularly interactions, is unknown. The LOSO and bootstrap analyses characterize within-dataset sensitivity but cannot substitute for independent replication, and nonsignificant results here do not establish the absence of an effect.

Third, the area-weighted grain aspect ratio was tested by a separate specimen-level ANOVA, outside the BH-FDR family applied to the four distribution-level descriptors. Its thermal-history result remains below 0.05 under a conservative 15-test Bonferroni calculation (approximate adjusted $p = 0.0015$), but that retrospective check does not replace a unified multiplicity analysis, and neither the number-weighted mean nor the number-weighted distribution showed a supported effect.

Fourth, the experiment used 1.5 and 2.5 mm^2 HIV solid copper wire from a single manufacturer with the insulation removed, and no chemical certificate or oxide analysis was available. Only conductor cross-section and the flame-remelting condition were varied; strand structure, copper composition and lot, insulation type, short-circuit current magnitude and duration, and fire heating and cooling histories were not. The descriptor responses cannot be presumed to transfer to those conditions.

Fifth, remelting was produced with a butane torch of approximately 1300 °C nominal flame temperature and typically required 50–70 s to reach the visual endpoint, but the internal metal temperature, heat flux, melt fraction, temperature gradient, solidification rate and cooling rate were not measured. The absence of internal temperature and melt-fraction data prevents discrimination between localized surface remelting, partial liquefaction and complete bulk remelting, so the conclusions apply to the flame-exposure condition defined by the operational metal-reflow endpoint rather than to a verified fully molten state. Fixed torch positioning and natural cooling in laboratory air did not ensure identical heat fluxes or cooling rates.

Sixth, EBSD was performed on one selected ROI within a single longitudinal section per specimen, and a verified specimen-specific record of ROI positions and sampled-area coverage was not available. Common inclusion and exclusion criteria improved consistency in the type of microstructure analyzed but do not establish that the selected ROI represents the entire melt-mark cross-section or the three-dimensional bead; spatial variation across the bead remains unquantified.

Seventh, the significant PERMDISP result for the number-weighted ASTM grain-size distribution ($p = 0.0357$) prevents attribution of its PERMANOVA terms solely to group-centroid differences, and PERMDISP was not repeated after small-grain filtering. The ASTM descriptor should therefore not be treated as an independent marker of remelting.

Eighth, the opposing circularity responses are supported by complementary specimen-level, distributional, quantile-shift and LOSO analyses of the same 20 specimens, but these do not independently verify the proposed cross-section-dependent solidification mechanism. Without quantitative grain-boundary perimeter metrics or three-dimensional measurements, the contributions of solidification conditions, two-dimensional section and ROI selection, and grain segmentation cannot be separated.

Ninth, the experiment compared only primary short-circuit marks and primary marks subsequently remelted by external flame. No secondary arc beads, alternative controlled fire-heating exposures or independently verified fire-scene specimens were included, so the specificity of the EBSD features for distinguishing these origins remains untested.

Future work should proceed in stages. First, independent replications should follow prespecified common acquisition, indexing, grain-reconstruction and reporting procedures, with multiple ROIs and repeated sections per specimen, retaining the independent melt-mark specimen as the unit of replication and planning sample size prospectively. Second, controlled experiments should systematically vary conductor cross-section and strand configuration, copper composition, insulation presence and type, short-circuit current waveform, duration and I^2t, and instrumented heating and cooling conditions, representing both reflow and non-reflow exposure. Third, the descriptors should be evaluated against four independently established history classes—primary short-circuit marks, primary marks remelted by flame, secondary arc beads formed during fire development, and marks subjected to other defined fire-heating conditions—and then in blinded studies on known-origin fire-scene specimens, reporting class-specific sensitivity and specificity and inter-laboratory reproducibility. None of these assessments was performed here.

5. Conclusions

This study examined the effects of post-short-circuit flame remelting on the EBSD microstructure of primary copper melt marks. The 2 × 2 factorial experiment involved 1.5 and 2.5 mm^2 solid copper conductors, with five independently prepared specimens in each thermal-history and conductor-size group. The response to remelting was not uniform across microstructural descriptors. Area-weighted grain diameter increased in both conductor sizes, with a larger relative increase at 2.5 mm^2. The maximum reconstructed grain diameter showed the same directional pattern. Area-weighted grain aspect ratio increased in both sizes, with its between-specimen variation decreasing to approximately one-third of the primary-group level, whereas circularity increased at 1.5 mm^2 but decreased at 2.5 mm^2. Three intragranular misorientation metrics showed no supported thermal-history effect. A post-reconstruction common-cutoff sensitivity analysis supported the area-weighted grain-diameter finding. In contrast, the number-weighted ASTM grain-size result was sensitive to the inclusion of smaller reconstructed grains, reflecting the dependence of number-weighted grain-size measures on the small-grain fraction.

These findings indicate that the microstructure of a copper melt mark recovered from a fire scene may reflect both its original electrical formation and later thermal exposure. The features therefore require interpretation alongside conductor cross-section, sampling and grain-reconstruction conditions, macroscopic observations, and independent scene evidence. Importantly, the remelted specimens were pre-existing primary marks exposed to flame; they were not secondary arc beads. This study did not include alternative fire-heating histories or independently verified fire-scene specimens, and it does not establish a validated classifier or chronology criterion. The results remain exploratory because the experiment used five independent specimens per group, two conductor sizes, one commercial wire source, one nominal short-circuit current and flame-remelting protocol, and one selected longitudinal EBSD region per specimen. Larger independent datasets, standardized and spatially replicated measurements, controlled thermal histories, and blinded external validation will be needed to assess transferability and forensic classification performance.

Author Contributions: Conceptualization, J.-H.K. and D.-D.L.; methodology, J.-H.K. and Y.-H.K.; software, J.-H.K.; validation, D.B. and C.C.; formal analysis, J.-H.K.; investigation, J.-H.K., D.B., C.C. and K.P.; resources, K.P. and J.J.; data curation, J.-H.K.; writing—original draft preparation, J.-H.K.; writing—review and editing, D.-D.L. and Y.-H.K.; visualization, J.-H.K.; supervision, D.-D.L.; project administration, D.-D.L.; funding acquisition, D.-D.L. All authors have read and agreed to the published version of the manuscript.

Funding: This research was funded by the National Fire Agency of Korea, administered by the Korea Evaluation Institute of Industrial Technology (KEIT), grant number RS-2025-03372990.

Institutional Review Board Statement: Not applicable.

Informed Consent Statement: Not applicable.

Data Availability Statement: The specimen-level EBSD descriptor distributions and summary statistics for all 20 specimens, the Wasserstein distance matrices, and the analysis scripts supporting the reported results are available from the corresponding author on reasonable request.

Acknowledgments: All acknowledged individuals have consented.

Conflicts of Interest: Authors Jeong-Hwan Kim, Daeryeong Baek, Chiwoo Choi, Kwangmuk Park and Jeongchay Jeon were employed by the Korea Electrical Safety Corporation. The remaining authors declare that the research was conducted in the absence of any commercial or financial relationships that could be construed as a potential conflict of interest.

Abbreviations

The following abbreviations are used in this manuscript:

AC	Alternating current
ANOVA	Analysis of variance
BH-FDR	Benjamini–Hochberg false discovery rate
CI	Confidence index
DC	Direct current
EBSD	Electron backscatter diffraction
FE-SEM	Field-emission scanning electron microscope
GAM	Grain average misorientation
GND	Geometrically necessary dislocation
HIV	Heat-resistant polyvinyl chloride-insulated building wire (wire designation)
IPF	Inverse pole figure
KAM	Kernel average misorientation
LOS	Local orientation spread
LOSO	Leave-one-specimen-out
OIM	Orientation imaging microscopy
PERMANOVA	Permutational multivariate analysis of variance
PERMDISP	Permutational analysis of multivariate dispersions
ROI	Region of interest
TEM	Transmission electron microscopy
W_1	1-Wasserstein distance

References

1. Huang, X.; Nakamura, Y. A Review of Fundamental Combustion Phenomena in Wire Fires. *Fire Technol.* **2020**, *56*, 315–360. [CrossRef]
2. Novak, C.J.; Stoliarov, S.I.; Keller, M.R.; Quintiere, J.G. An Analysis of Heat Flux Induced Arc Formation in a Residential Electrical Cable. *Fire Saf. J.* **2013**, *55*, 61–68. [CrossRef]
3. Weinschenk, C.; Madrzykowski, D.; Courtney, P. Impact of Flashover Fire Conditions on Exposed Energized Electrical Cords/Cables. *Fire Technol.* **2020**, *56*, 959–991. [CrossRef]
4. Erlandsson, R.; Strand, G. An Investigation of Physical Characteristics Indicating Primary or Secondary Electrical Damage. *Fire Saf. J.* **1985**, *8*, 97–103. [CrossRef]
5. Lee, E.-P.; Ohtani, H.; Matsubara, Y.; Seki, T.; Hasegawa, H.; Imada, S.; Yashiro, I. Study on Discrimination between Primary and Secondary Molten Marks Using Carbonized Residue. *Fire Saf. J.* **2002**, *37*, 353–368. [CrossRef]
6. Chen, C.Y.; Ling, Y.C.; Wang, J.T.; Chen, H.Y. SIMS Depth Profiling Analysis of Electrical Arc Residues in Fire Investigation. *Appl. Surf. Sci.* **2003**, *203–204*, 779–784. [CrossRef]
7. Xie, D.; Wang, W.; Lv, S.; Deng, S. Visual and Oxide Analysis for Identification of Electrical Fire Scene. *Forensic Sci. Int.* **2018**, *285*, e21–e24. [CrossRef]
8. Wright, S.A.; Loud, J.D.; Blanchard, R.A. Globules and Beads: What Do They Indicate about Small-Diameter Copper Conductors That Have Been through a Fire? *Fire Technol.* **2015**, *51*, 1051–1070. [CrossRef]
9. Liu, K.-H.; Shih, Y.-H.; Chen, G.-J.; Chou, J.-M. Microstructural Study on Molten Marks of Fire-Causing Copper Wires. *Materials* **2015**, *8*, 3776–3790. [CrossRef]
10. Deng, J.; Li, Y.; Lü, H.-F.; Wang, W.-F.; Bai, L.; Shu, C.-M. Metallurgical Analysis of the 'Cause' Arc Beads Pattern Characteristics under Different Short-Circuit Currents. *J. Loss Prev. Process Ind.* **2020**, *68*, 104339. [CrossRef]
11. Yu, Z.; Chen, S.; Deng, J.; Xu, X.; Wang, W. Microstructural Characteristics of Arc Beads with Overcurrent Fault in the Fire Scene. *Materials* **2020**, *13*, 4521. [CrossRef]
12. Park, J.; Kang, J.-H.; Lee, E.P.; Ko, Y.H.; Bang, S.B. New Approach to Distinguish Copper Molten Marks Based on Quantitative Microstructure Analysis Using Electron Backscatter Diffraction. *Fire Technol.* **2021**, *57*, 1667–1682. [CrossRef]
13. Park, J.; Kang, J.-H.; Jang, H.-S.; Ko, Y.H.; Bang, S.B. Potential Method to Distinguish Copper Molten Marks Using Boundary and Grain Characteristics. *Materials* **2022**, *15*, 4534. [CrossRef]
14. Park, J.; Kang, J.-H.; Park, J.; Ko, Y.H.; Bang, S.B. Discrimination of Copper Molten Marks through a Fire Reproduction Experiment Using Microstructure Features. *Materials* **2022**, *15*, 8206. [CrossRef]
15. Wang, G.; Chen, T.; Wang, Z.; Gao, Z.; Mi, W. Beads and Globules from Fires: Can They Be Differentiated through Metallurgical Analysis Based on Machine Learning Algorithms? *Fire* **2022**, *5*, 123. [CrossRef]
16. Lü, H.-F.; Deng, J.; Li, Y.; Wang, W.-F.; Bai, L.; Shu, C.-M. Influence of Thermal Environment on Metallographic Structure Characteristics of the Electric Arc Bead Pattern. *J. Loss Prev. Process Ind.* **2021**, *70*, 104426. [CrossRef]

17. Gudym, V.; Mykhalichko, B.; Nazarovets, O.; Gavryliuk, A. The Effect of Short Circuits and Flame Temperature Modes on the Change in the Microstructure of Copper in Automotive Wiring. *Eng. Fail. Anal.* **2022**, *136*, 106198. [CrossRef]
18. Wang, W.; Zhao, X.; Liu, Q.; Ji, X.; Yang, Z.; Gui, X.; Li, Z.; Wang, L. Study on Quantitative Metallographic Analysis Method of Copper Wire Melt Trace under Short-Circuit and Fire Conditions. *J. Therm. Anal. Calorim.* **2023**, *148*, 12145–12158. [CrossRef]
19. Hong, S.; Bang, S.-B.; Bang, J.-H.; Park, J.; Min, K.-D.; Lee, J.-S. Analysis of Visual Characteristics of Short-Circuited Arc Sites. *Fire Technol.* **2023**, *59*, 559–580. [CrossRef]
20. Yu, F.; Wang, S.; Tang, K.; Lin, Y.; Wang, S.; Zhang, Y. Research Progress on the Fire Characteristics of Electric Cables and Wires. *Fire* **2024**, *7*, 186. [CrossRef]
21. Sachana, S.; Morishita, K.; Miyahara, H. Microstructural Examination of Molten Marks on Copper Wire for Fire Investigation. *Forensic Sci.* **2023**, *3*, 12–19. [CrossRef]
22. Wang, W.; Ji, X.; Zhang, F.; Zhao, X.; Gui, X.; He, D.; Wang, L. Study on the Microstructure Characteristics of Melting Marks in Copper-Clad Aluminum Wires under Overcurrent Faults. *J. Therm. Anal. Calorim.* **2024**, *149*, 345–357. [CrossRef]
23. Park, K.; Kim, J.-H.; Choi, C.; Baek, D.; Jeon, J. Reassessment of the Validity of Primary Arc Bead Generation Methods: Ignition Experiments and EBSD Analysis. *Fire* **2026**, *9*, 461. [CrossRef]
24. *Standard's ASTM E112-13*; Standard Test Methods for Determining Average Grain Size. ASTM International: West Conshohocken, PA, USA, 2021. [CrossRef]
25. Ramdas, A.; García Trillos, N.; Cuturi, M. On Wasserstein Two-Sample Testing and Related Families of Nonparametric Tests. *Entropy* **2017**, *19*, 47. [CrossRef]
26. Anderson, M.J. A New Method for Non-Parametric Multivariate Analysis of Variance. *Austral Ecol.* **2001**, *26*, 32–46. [CrossRef]
27. Anderson, M.J. Distance-Based Tests for Homogeneity of Multivariate Dispersions. *Biometrics* **2006**, *62*, 245–253. [CrossRef] [PubMed]
28. Benjamini, Y.; Hochberg, Y. Controlling the False Discovery Rate: A Practical and Powerful Approach to Multiple Testing. *J. R. Stat. Soc. B* **1995**, *57*, 289–300. [CrossRef]
29. Heidelbach, F.; Wenk, H.-R.; Chen, S.R.; Pospiech, J.; Wright, S.I. Orientation and Misorientation Characteristics of Annealed, Rolled and Recrystallized Copper. *Mater. Sci. Eng. A* **1996**, *215*, 39–49. [CrossRef]
30. Tsai, D.C.; Hwang, W.S. Numerical Simulation of the Solidification Processes of Copper during Vacuum Continuous Casting. *J. Cryst. Growth* **2012**, *343*, 45–54. [CrossRef]
31. Kamaya, M. Correction of Step Size Dependency in Local Misorientation Obtained by EBSD Measurements: Introducing Equidistant Local Misorientation. *Ultramicroscopy* **2024**, *259*, 113928. [CrossRef] [PubMed]

Disclaimer/Publisher's Note: The statements, opinions and data contained in all publications are solely those of the individual author(s) and contributor(s) and not of MDPI and/or the editor(s). MDPI and/or the editor(s) disclaim responsibility for any injury to people or property resulting from any ideas, methods, instructions or products referred to in the content.